Journal of Bio- and Tribo-Corrosion (2023) 9:62
https://doi.org/10.1007/s40735-023-00779-0

The Effect of Annealing Temperature and Immersion Time on the Active–Passive Dissolution of Biomedical $Ti_{70}Zr_{20}Nb_{7.5}Ta_{2.5}$ Alloy in Ringer′s Solution

Nobl F. El Boraei[1] · **Magdy A. M. Ibrahim**[2] · **Sayed S. Abd El Rehim**[2] · **Ibrahim H. Elshamy**[2]

Received: 22 December 2022 / Revised: 26 March 2023 / Accepted: 20 June 2023 / Published online: 5 July 2023

Abstract

Because of their superior biocompatibility, chemical stability, and mechanical strength, Ti and Ti-based alloys are commonly utilized in orthopedic dentistry. In Ringer′s solution (RS), the corrosion behavior of the $Ti_{70}Zr_{20}Nb_{7.5}Ta_{2.5}$ alloy was examined as an alternative potential material for Ti and Ti_6Al_4V (T_6A_4V) in medical applications. The corrosion resistance was evaluated utilizing potentiodynamic polarization curves (PPCs), electrochemical impedance spectroscopy (EIS), and open-circuit potential techniques (OCP), supplemented by XRD and SEM surface analysis. The $T_{70}Z_{20}N_{7.5}T_{2.5}$ alloy has the highest resistance to corrosion since it has the most stable passive state in addition to the lowest corrosion current ($I_{corr} = 11.8\ \mu A\ cm^{-2}$) and lowest CR (6.1 mpy) in comparison with that of T_6A_4V ($I_{corr} = 13.7\ \mu A\ cm^{-2}$, CR = 7.13 mpy) and Ti ($I_{corr} = 29.5\ \mu A\ cm^{-2}$, CR = 15.3 mpy). Furthermore, it was also looked at how different annealing temperatures (600, 800, and 1000 °C) and immersion times (one, two, and three weeks) affected the corrosion behavior of $T_{70}Z_{20}N_{7.5}T_{2.5}$. In comparison to the other samples, the $T_{70}Z_{20}N_{7.5}T_{2.5}$ alloy annealed at 800 °C demonstrated superior resistance to corrosion (the lowest $I_{corr} = 1.53 \times 10^{-6}\ A\ cm^{-2}$) and $I_{pass} = 0.009\ mA\ cm^{-2}$. While that annealed at 1000 °C has the lowest resistance to corrosion (highest $I_{corr} = 4.49 \times 10^{-5}\ A\ cm^{-2}$ and $I_{pass} = 0.611\ mA\ cm^{-2}$) as a result of the passive layer dissolution. The passive film is composed of an inner and outer oxide layer, according to the EIS measurements. Meanwhile, the PPCs data demonstrate that the resistance to corrosion of the alloy is higher without immersion than it is with immersion and for a shorter immersion time. It was found that the $T_{70}Z_{20}N_{7.5}T_{2.5}$ system consisted of α and β phases. An X-ray structural study indicated a mixture of body-centered cubic β-Ti and hexagonal close-packed α-Ti (main phase, with a grain size of about 5.35 nm). Therefore, among all the materials evaluated in this work, the $T_{70}Z_{20}N_{7.5}T_{2.5}$ alloy can be considered a promising material suitable for use as a biomaterial.

Keywords Ringer's solution · Biomedical $Ti_{70}Zr_{20}Nb_{7.5}Ta_{2.5}$ alloy · Passivity · Annealing · Immersion time

1 Introduction

Ti and Ti-based alloys are widely utilized for orthopedic and dental purposes as a result of their superior chemical stability, mechanical strength, and biocompatibility [1–4]. For surgical implants, Ti_6Al_4V, TiNi, and Ti_6Al_7Nb alloys are currently the most frequently utilized. Nevertheless, the toxicity of aluminum and vanadium as well as the high sensitivity of Ni leads to the formation of non-toxic Ti-based alloys [5–8]. Several binary or ternary Ti-based alloys have reportedly been used to create implants, including TiNb [9], TiTa [10], TiZr [11], $Ti_{35}Nb_7Zr_5Ta$ [12], and $Ti_{13}Zr_{13}Nb$ [13]. One of them, $Ti_{13}Nb_{13}Zr$ has recently gained attention due to its superbly comprehensive properties, which include superior corrosion resistance and a lower elastic modulus (70 GP) [6, 7]. To improve the compatibility and interaction between the implanted alloys and the tissues, the porosity and surface shape of the alloys should be modified. However, the sintering environment had a significant impact on the pore size and alloy homogeneity [14]. The most crucial characteristics for an implant in the human body are biocompatibility and resistance to corrosion, which increase the

---

✉ Magdy A. M. Ibrahim
magdyibrahim@sci.asu.edu.eg

[1] Department of Chemistry, Faculty of Education, Ain Shams University, Roxy, Cairo 11711, Egypt

[2] Department of Chemistry, Faculty of Science, Ain Shams University, Abbassia, Cairo 11566, Egypt

usage of alloys as biomaterials [15]. Niobium (Nb) addition may improve a material's ability to resist corrosion [16]. Acceptable mechanical strength is displayed by zirconium (Zr) [17], and in vivo research has shown that zirconium implants have good osteointegration [18, 19]. Tantalum (Ta) has more resistant to corrosion than Nb due to the increase in its oxide stability [20, 21]. Both the biocompatibility of Ta and its superior corrosion resistance have undergone rigorous evaluation [22]. TiZrNbTa alloys are therefore anticipated to have great corrosion resistance and excellent biocompatibility due to the unique properties of Ta, Zr, and Nb. On the other hand, Zr, Nb, and Ta were chosen as intensification elements because they are toxicology-free elements that have been thoroughly studied and found to have no undesirable effects on tissue [23]. Comprehensive ion production from a prosthesis can have undesirable biological effects that cause mechanical failure of the device. In general, it is preferable to use corrosion-resistant materials to reduce the amount of metal ions released, which mostly rely on the stable passive film that forms on the alloy surface to act as a barrier between the alloy substrate and the bio-environment [24]. Even so, other protection techniques can be applied [25–27]. The literature did not have any thorough information regarding the corrosion behavior of the $T_{70}Z_{20}N_{7.5}T_{2.5}$ alloy in a RS. The aim of the research was to examine the $T_{70}Z_{20}N_{7.5}T_{2.5}$ corrosion behavior compared with Ti and T_6A_4V in RS using various electrochemical techniques: PPCs, EIS, and OCP measurements. Also, the corrosion behavior of the $T_{70}Z_{20}N_{7.5}T_{2.5}$ alloy in RS at different immersion times and at different annealing temperatures was studied, along with the passive film structure analysis by an X-ray diffraction analysis.

2 Experimental Details

The corrosion behavior of the three materials Ti, T_6A_4V, and $T_{70}Z_{20}N_{7.5}T_{2.5}$ in RS was compared using an electrochemical analysis (their compositions are given in Table 1). Using epoxy cold resin mounting of alloys, the Ti, T_6A_4V, and $T_{70}Z_{20}N_{7.5}T_{2.5}$ electrodes were prepared, allowing 1.0 cm^2 of the electrode surface to be exposed to RS. In electrochemical studies, the Ti, T_6A_4V, and $T_{70}Z_{20}N_{7.5}T_{2.5}$ electrodes were employed as the working electrodes (Japan Coating Center Co. Ltd., Kanagawa, Japan, provided the electrode specimens). The electrode is mechanically polished with fine sandpaper of various grades, beginning with 500, moving up to 800, and ending with 1200, before being washed with acetone and distilled water. After activating the electrode in 1.0-M hydrogen fluoride for 1.0 min, it is carefully cleaned with double-distilled H_2O. The counter electrode was a platinum electrode. For all potential measurements, a reference electrode was silver/silver chloride. For each experiment, measurements were made at 37 °C using freshly generated RS as the electrolyte to simulate the conditions that a biological component might encounter. The chemical components of RS were dissolved in 1.0 L of distilled H_2O:9.00-g sodium chloride, 0.40-g potassium chloride, 0.20-g sodium bicarbonate, and 0.25-g calcium chloride dissolved in 1.0 L of distilled H_2O [23]. All solutions were freshly prepared from analytical-grade chemicals and doubly distilled water. The solution was kept at pH 7.4. In an electric heat furnace, the annealing procedure was perfected at temperatures of 600 °C, 800 °C, and 1000 °C. Two hours were spent holding the substance, and air conditioning was used to cool it.

The electrochemical investigations used a 1000 Gamry Instrument Potentiostat/Galvanostat/ZRA. All the electrochemical parameters were derived using the Echem Analyst software supplied by Gamry Instruments. The PPCs were done using a voltage range of -1.2 to $+3.0$ V and a 5-mV s^{-1} scan rate. The EIS diagrams were plotted after 1800s of immersion in a RS with a frequency range from 100,000 Hz to10.0 mHz with an amplitude of 5 mV peak to peak. The tests were done after 30 min of immersion. The electrochemical experiments were evaluated in accordance with the accepted test procedure to identify the tiny implant's sensitivity to corrosion. Each test was carried out twice. The samples surface morphology under test was investigated utilizing the scanning electron microscopy (SEM) model JEOL JEM-1200EX II Electron Microscope. An X-ray diffraction analysis was applied (Panalytical Empyrean, the Netherlands) with a CuKa radiation ($\lambda = 1.54045$ Å) at an accelerating voltage of 40 kV and current 35 mA.

3 Results and Discussion

3.1 Corrosion Resistance Resulted from PPCs

Figure 1 shows PPCs of $T_{70}Z_{20}N_{7.5}T_{2.5}$, T_6A_4V, and Ti electrodes in a RS, at 37 °C with a 5-mVs^{-1} scan rate. The related corrosion parameters obtained are shown in Table 2.

Table 1 Chemical composition (wt. %) of $T_{70}Z_{20}N_{7.5}T_{2.5}$, T_6A_4V, and Ti

Materials	Ti	Zr	Nb	Ta	Al	V	C	N	Si
$T_{70}Z_{20}N_{7.5}T_{2.5}$	52.19	25.43	10.45	7.09	0.39	0.32	2.55	1.58	–
T_6A_4V	90.32	–	–	–	4.28	4.5	0.81	–	0.09
Ti	98.9	–	–	–	0.3	–	0.68	–	0.12

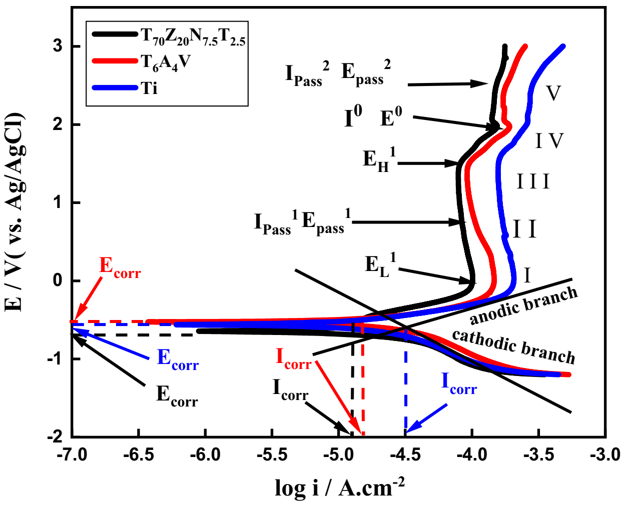

Fig. 1 Potentiodynamic polarization curves of $T_{70}Z_{20}N_{7.5}T_{2.5,}$ T_6A_4V, and Ti electrodes in a RS recorded with a sweep rate of 5 mVs^{-1} at 37 °C

There are five zones (I-V) in the PPCs of the $T_{70}Z_{20}N_{7.5}T_{2.5}$, T_6A_4V, and Ti. Because the Ti element and alloying elements are oxidized into ions of varying valences and the production of the passive layers happens simultaneously with the reactions, the first region (I) demonstrates that the electrodes are in the active–passive state. As a result of reactions dominating passive layer production, the current density rises as potential rises. The current densities ($I_{pass}{}^1$) stay very stable as the potential increases in the zone (II), reaching about 87.7, 98.28, and 160.3 μA cm^{-2} for $T_{70}Z_{20}N_{7.5}T_{2.5}$, T_6A_4V, and Ti, respectively. This depicts that as the voltage approached $E_L{}^1$ (the low limit voltage in the first passive zone) (II), the passive layers gradually produced on the electrode surface. For the three materials $T_{70}Z_{20}N_{7.5}T_{2.5}$, T_6A_4V, and Ti at various voltages ($E_H{}^1$), about 1.46, 1.47, and 1.55 V correspondingly, with an increase in the voltage, the current density rises (III). This could be accounted for by the reality that chloride ions from the RS destroyed the passive layers. Some electrode areas that had previously been passively protected from corrosion by films are exposed to the solution once again, and the elements of alloying like Zr, Al, and Ti participate in the charge transfer when the voltage is raised. The highest current densities (I°) (region IV), 132.4, 189.3, and 262.4 mA cm^{-2}, are reached for $T_{70}Z_{20}N_{7.5}T_{2.5}$, T_6A_4V, and Ti when the potentials E° (the voltage corresponding to the greatest current density) increase to approximately 1.99, 2.04, and 2.06 V, respectively. As the voltage increases and gradually replaces the reactions, the breakdown parts on the passive films are restored.

Restoring the breakdown parts on the passive layers continues along with the voltage increase and gradually supplants the reactions. Ultimately, the three electrodes, $T_{70}Z_{20}N_{7.5}T_{2.5}$, T_6A_4V, and Ti, have respective current densities ($I_{pass}{}^2$) (region V) of 134.1, 176.9, and 276.9 μA cm^{-2}, all of which are quite steady values. This indicates a formal transition into the re-passive condition for the electrodes.

The potentiodynamic polarization approach can be used to analyze the passive behaviors to determine the relative stability of the passive layers in the specific medium as well as the passivity tendency of the materials. Three parameters, including ($E_L{}^1$) for the first passive zone and I° and E° for the re-passive zone, are correlated to the previous. $E_L{}^1$ distinguishes the difficulty in the first passive case. The system can become passive more easily, and the closer the materials are to the E_{corr} (corrosion potential) the more quickly they are protected from corrosion.

The regions exposed to localized corrosion are small as I° is low, and the restoration times for passive films are very fast. Therefore, from the active stage to the re-passive stage, the electrodes are easier to convert. In a similar vein, when E° is low relative to I°, it is favorable for the system to enter the re-passive state. As can be seen in Fig. 1 and Table 2, the $T_{70}Z_{20}N_{7.5}T_{2.5}$ has the lowest values of $E_L{}^1$, E°, and I° in comparison to the other materials investigated. Based on the results already mentioned, it can be said that $T_{70}Z_{20}N_{7.5}T_{2.5}$ enters the passive stage more readily.

Two factors—the voltage range and the I_{pass} in the passive stage—distinguish the stability of passive films. The more expansive the voltage range, the harder it is for the passive layers to transfer from the passive stage to the active stage. Furthermore, the passive coatings appear to be more

Table 2 Electrochemical parameters obtained for a Ti, T_6A_4V alloy, and $T_{70}Z_{20}N_{7.5}T_{2.5}$ alloy in a RS at 37 °C

Material	I_{Corr} μA cm^{-2}	E_{corr} V	$E_L{}^1$ V	$E_H{}^1$ V	E° V	$E_L{}^2$ V	$I_{pass}{}^1$ μA cm^{-2}	I° μA cm^{-2}	$I_{pass}{}^2$ μA cm^{-2}	CR mpy
$T_{70}Z_{20}N_{7.5}T_{2.5}$	11.8	−0.558	0.336	1.46	1.99	2.13	87.7	132.4	134.1	6.10
T_6A_4V	13.7	−0.524	0.606	1.47	2.04	2.14	98.28	189.3	176.9	7.13
Ti	29.5	−0.786	0.711	1.55	2.06	2.16	160.3	262.4	276.9	15.3

E_{corr} is the corrosion potential, I_{corr} is the corrosion current density, $E_L{}^1$ and $E_H{}^1$ are the low limit and high limit potentials in the first passive region, respectively, $I_{pass}{}^1$ is the current density in the first passive region, $E°$ is the potential in correspondence with the highest current density, I ° is the highest current density during the whole scanning range, $E_L{}^2$ is the low limit potential in the re-passive region, and ($I_{pass}{}^2$) is the current density in the re-passive region stable because their dissolution rate is comparatively slow and their I_{pass}^{1}, I_{pass}^{2} values are low, regardless of whether they are in the primary passive stage or the re-passive stage, suggesting that the passive layers are more stable. The first passive area voltage ranges are 1.124, 0.864, and 0.839 V for $T_{70}Z_{20}N_{7.5}T_{2.5}$, T_6A_4V, and Ti, respectively. Certainly, $T_{70}Z_{20}N_{7.5}T_{2.5}$ has the widest potential range. Similar to this, $T_{70}Z_{20}N_{7.5}T_{2.5}$ also exhibits low passive current densities, with values of 87.7 and 134.1 mA cm^{-2} in the initial passive and re-passive regions, respectively.

According to the study presented above, the passive layer that has developed on the $T_{70}Z_{20}N_{7.5}T_{2.5}$ surface is the most stable among the remnants. Because of the presence of alloying elements, like vanadium, aluminum, zirconium, niobium, and tantalum, that help to reduce anode activity and promote passivity, $T_{70}Z_{20}N_{7.5}T_{2.5}$ and T_6A_4V alloys have better passive characteristics than Ti.

3.2 Corrosion Resistance Resulted from EIS

The Nyquist plots of the samples $T_{70}Z_{20}N_{7.5}T_{2.5}$, T_6A_4V, and Ti after 1800s of immersion in a RS at 37 °C are shown in Fig. 2a. Due to the frequency dispersion, it is revealed that all of the diagrams are portions of the imperfect semicircles [28]. It is evident from impedance diagrams' depressed semi-circular shape that a charge transfer process controls how readily titanium and its alloys corrode.

According to Bode plots (Fig. 2b), the Z_{mod} value (modulus of impedance) for $T_{70}Z_{20}N_{7.5}T_{2.5}$ (28.18 kΩ cm^2) is larger than that for T_6A_4V alloy (16.60 kΩ cm^2) and Ti (6.92 kΩ cm^2), respectively. The high impedance values show the typical passive film capacitive response behavior [29–33]. The highest Z_{mod} value for $T_{70}Z_{20}N_{7.5}T_{2.5}$ alloy in RS suggests improved resistance to corrosion of the spontaneous oxide layer compared to T_6A_4V alloy and Ti. Additionally, the highest value of phase angle for the $T_{70}Z_{20}N_{7.5}T_{2.5}$ alloy (-76.88) compared to the T_6A_4V alloy (-75.85) and Ti (-67.02) shows that the $T_{70}Z_{20}N_{7.5}T_{2.5}$ alloy may have a passive film protecting it in the RS. Consequently, two layers of passive film were modeled: the outer porous layer, which is in charge of the dissolution processes through the passive film, and the inner compact barrier layer, which is in charge of the alloy's resistance [29–34].

An electric equivalent circuit with two time constants was used to describe the dual-outer/inner oxide layers [35]. The electrical circuit models were used to analyze the impedance spectra collected at the OCP, and the results were successfully used to fit the whole set of data for all materials under test ($T_{70}Z_{20}N_{7.5}T_{2.5}$, T_6A_4V, and Ti) utilizing the equivalent circuit (EC) shown in Fig. 3. The elements of this equivalent circuit are as follows: Rs is the resistance of electrolyte, R_p and CPE_p are the resistance and capacitance of the porous oxide film, and R_b and CPE_b are the resistance and capacitance of the barrier oxide film [29–34]. To obtain effective compatibility between the results of the simulations and those of the experiments, pure capacitors were replaced with constant phase elements (CPE) in the fitting process.

The impedance of CPE was determined by [35]:

$$Z_{CPE} = \left[C(j\omega)^{n}\right]^{-1}, \tag{1}$$

where C is the capacitance, ω is the angular frequency, and n is the non-uniform current distribution attributed to surface inhomogeneity or roughness. Table 3 displays the

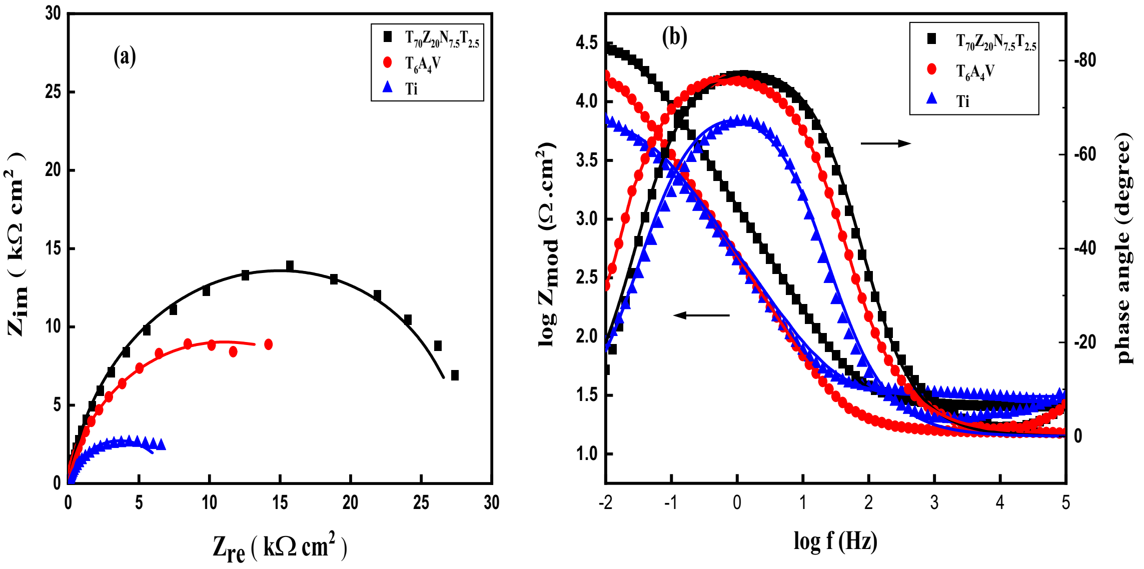

Fig. 2 Nyquist plots (**a**) and Bode plots (**b**) of EIS data of $T_{70}Z_{20}N_{7.5}T_{2.5}$, T_6A_4V, and Ti electrodes after 30 min of immersion in a RS at 37 °C

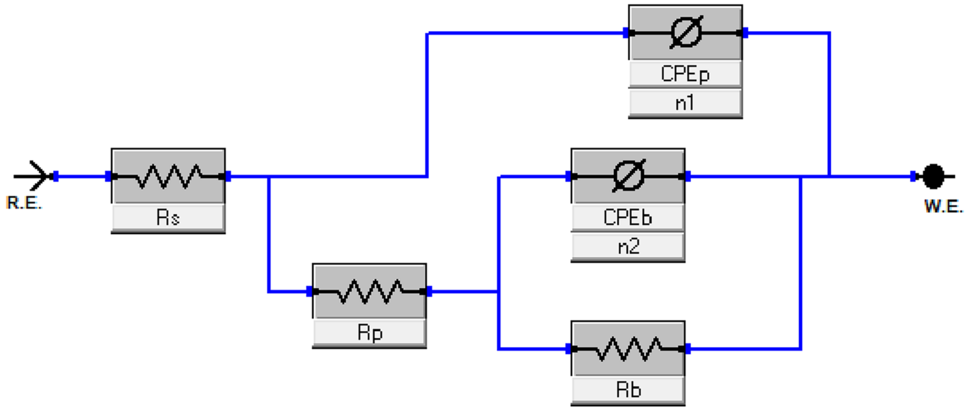

Fig. 3 The equivalent circuit used for the EIS data fitting

Table 3 Fitting parameters of EIS obtained for a $T_{70}Z_{20}N_{7.5}T_{2.5}$ alloy, T_6A_4V alloy, and Ti in a RS at 37 °C

Material	R_s (Ω cm^2)	R_b (kΩ cm^2)	CPE_b (F cm^2 Hz^{1-n1})	n_1	R_p (kΩ cm^2)	CPE_p (F cm^2 Hz^{1-n2})	n_2
$T_{70}Z_{20}N_{7.5}T_{2.5}$	44.56	31.59×10^3	45.60×10^{-6}	0.842	45.79	147.2×10^{-6}	0.895
T_6A_4V	38.90	28.46×10^3	54.20×10^{-6}	0.856	34.15	279.2×10^{-6}	0.888
Ti	34.12	17.14×10^3	96.28×10^{-6}	0.754	29.24	510.7×10^{-6}	0.827

main parameters for all studied samples (R_s, R_b, CPE_b, R_p, and CPE_p) of the recommended EC. According to the fitting parameters, the inner film has a stronger resistance to charge and species transport than the outer film, which is confirmed by the largest values of R_b relative to R_p. The CPE_p values are superior to the CPE_b values, suggesting that the barrier layer is what gives the corrosion resistance. These data prove that the protection offered by the passive film is mostly attributed to the inner compact film [36]. As a result, the $T_{70}Z_{20}N_{7.5}T_{2.5}$ alloy was discovered to have the highest resistance of the inner compact film. The n_1 and n_2 values are lower than 1. This refers to faults caused by surface heterogeneity, roughness, the creation of porous layers, and adsorption films [37].

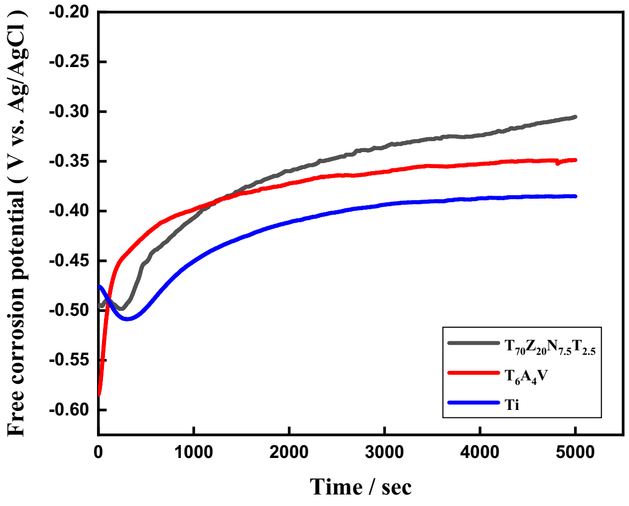

Fig. 4 Open-circuit potential behavior as a function of time of $T_{70}Z_{20}N_{7.5}T_{2.5}$, T_6A_4V, and Ti electrodes in a RS at 37 °C

3.3 Corrosion Resistance Resulted from OCP

The variations in the free corrosion potential with time for $T_{70}Z_{20}N_{7.5}T_{2.5}$, T_6A_4V, and Ti samples in a RS at 37 °C are shown in Fig. 4. The nobility of the materials can be compared using the OCP values [38, 39]. It is common knowledge that a high open-circuit potential value corresponds to a strong resistance to corrosion. In the case of Ti, the potential decreased for a short time (300 s) (the dissolution of the natural oxide layer), then quickly rose in the OCP to the greater positive potentials to indicate its capability to re-passivate, and a steady-state value of − 0.48 V was eventually reached [40, 41]. In the case of T_6A_4V, the potential appears to be more negative (− 0.58 V). However, with time, it starts to increase gradually to more positive potentials, indicating its ability to re-passivate, and a steady-state value at − 0.35 V was eventually reached. After a short time of decreasing potential (200 s), in comparison with Ti, the OCP values became more positive with time for $T_{70}Z_{20}N_{7.5}T_{2.5}$. This indicates the rapid re-passivation and reaching a steady-state potential of − 0.30 V. According to this characteristic, protective passive films quickly form and serve as a barrier to metal disintegration, reducing the rate of corrosion. The results for PPCs are consistent with the steady-state potential of OCP, which highlights the order in which the long-term corrosion resistance of the samples reduces as follows: $Ti_{70}Zr_{20}Nb_{7.5}Ta_{2.5} > TiAlV > Ti$.

3.4 Effect of Annealing Temperature

For titanium alloys, there are numerous different kinds of heat treatments. Annealing, aging, deformation heat treating, and chemical heat treating are frequently used processes. Different titanium alloys can benefit from annealing, which primarily serves to reduce stress, enhance alloy plasticity, and stabilize the structure. The recrystallization temperature should be higher than the stress-relieving annealing temperature, which should be in the extent of 450 to 650 °C. The characteristics of the alloy will decrease if the temperature rises above the phase transition point. Therefore, our studied alloy sample was subjected to annealing in the temperature range of 600–1000 °C.

3.4.1 Corrosion Resistance Resulted from PPCs

Figure 5 shows the PPCs of the $T_{70}Z_{20}N_{7.5}T_{2.5}$ alloy without and with annealing at various temperatures in a RS with a 5-mVs^{-1} scan rate. The polarization curves for the unannealed and annealed samples at 600, 800, and 1000 °C showed active–passive behavior. The polarization curves without annealing are pushed toward a less noble potential, suggesting that the resistance to corrosion of the $T_{70}Z_{20}N_{7.5}T_{2.5}$ sample reduces. Table 4 displays the electrochemical parameters deduced from the polarization curves. The sample annealed at 1000 ºC showed the lowest E_{corr} (-5.51×10^{-1} V), the largest I_{corr} (4.49×10^{-5} A cm^{-2}), the worst resistance to corrosion, and the largest CR (corrosion rate) (23.30 mpy). However, the alloy annealed at 800ºC exhibited the highest E_{corr} (-2.45×10^{-1} V), the lowest I_{corr} (1.53×10^{-6} A cm^{-2}), the best resistance to corrosion, and the least CR (0.795 mpy). The E_{corr} (-3.13×10^{-1} V), the I_{corr} (2.49×10^{-6} A cm^{-2}) and the CR (1.292 mpy) of the sample that was annealed at 600ºC were between those of the annealed samples at 800 and 1000 °C, as well as the unannealed sample ($E_{corr} = -6.46 \times 10^{-1}$ V, $I_{corr} = 1.18 \times 10^{-5}$, and CR = 6.10 mpy). Additionally, the I_{pass} of the $T_{70}Z_{20}N_{7.5}T_{2.5}$ sample after annealing at various temperatures was seen to vary after the activation–passivation transition. The sample that was annealed at 1000ºC had the highest I_{pass} (0.611 mA cm^{-2}), followed by the sample that was annealed at 600 °C (0.036 mA cm^{-2}). The sample that was annealed at 800 °C had the lowest passivation current density (0.009 mA cm^{-2}), although the difference was extremely tiny.

Table 4 Electrochemical parameters obtained for a $T_{70}Z_{20}N_{7.5}T_{2.5}$ alloy in a RS annealed at different temperatures

Temperature °C	I_{Corr} A cm^{-2}	$-E_{Corr}$ V	I_{pass} mA cm^{-2}	CR mpy
Unannealed	1.18×10^{-5}	0.558	0.114	6.10
600	2.49×10^{-6}	0.313	0.036	1.292
800	1.53×10^{-6}	0.245	0.009	0.795
1000	4.49×10^{-5}	0.551	0.611	23.30

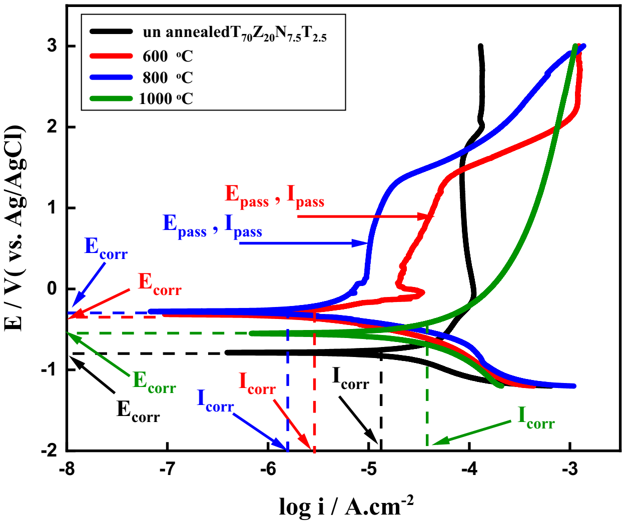

Fig. 5 Potentiodynamic polarization curves of $T_{70}Z_{20}N_{7.5}T_{2.5}$ alloy in a RS after annealing at different temperatures with a sweep rate of 5 mVs^{-1}

3.4.2 Corrosion Resistance Resulted from EIS

In Figs. 6a and b, the EIS examinations of the $T_{70}Z_{20}N_{7.5}T_{2.5}$ alloy at the OCP with 30 min of immersion in a RS without and with annealing at various temperatures are shown. According to Nyquist plots (Fig. 6a), the capacitive semicircle value of the unannealed sample is greater than that of the annealed sample at 1000 °C but lower than that of the annealed sample at 600 and 800 °C. The above findings demonstrate that the resistance to corrosion of the $T_{70}Z_{20}N_{7.5}T_{2.5}$ sample without annealing and the annealed sample at a crucial temperature (1000 °C) reduces attributed to the dissolution of the passive layer, whereas the resistance to corrosion of the annealed sample at a crucial temperature rises (up to 800 °C). In Bode plots (Fig. 6b), as the annealing temperature rises from 600 to 800 °C, the Z_{mod} values sharply increase from 32.36 to 63.06 kΩ cm^2, and the maximum phase angles rise from − 62.08 to − 71.45°, but at very high annealing temperatures (1000 °C), the Z_{mod} values and maximum phase angles sharply decrease to 3.311 kΩ cm^2 and − 17.38°, respectively, as they move slightly to a higher-frequency zone. These data indicate that at high annealing temperatures (600, 800 °C) the oxide layer on the surface of the alloy has high resistance, but at a higher annealing temperature 1000 °C, the oxide film suffers from the dissolution process. It was found that the EC

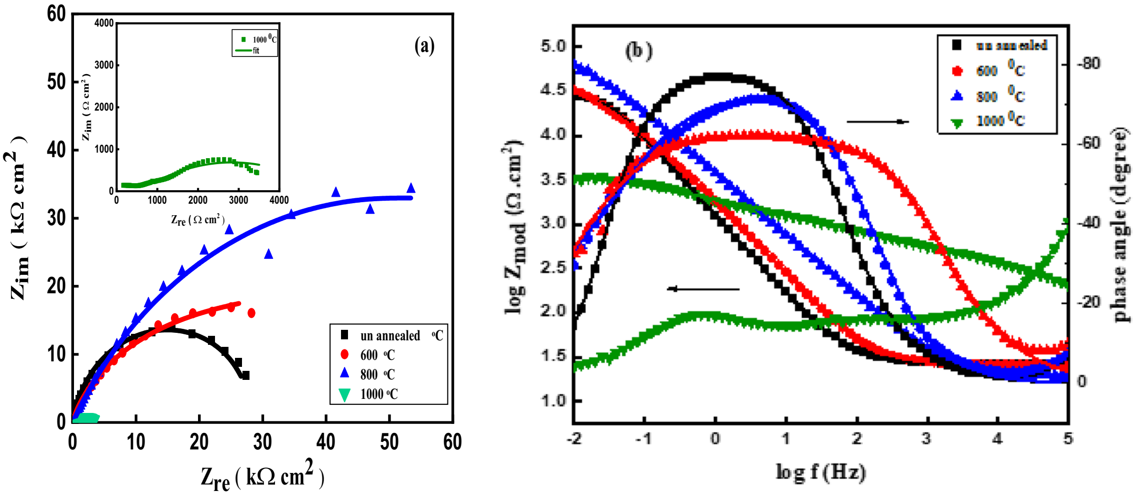

Fig. 6 Nyquist diagrams (**a**) and Bode plots (**b**) of $T_{70}Z_{20}N_{7.5}T_{2.5}$ at open-circuit potential in a RS after annealing at different temperatures

shown in Fig. 3 could satisfactorily match the entire set of data for the $T_{70}Z_{20}N_{7.5}T_{2.5}$ alloy. According to fitting parameters, the values of R_p and R_b rise as the annealing temperature rises (600–800 °C), indicating that the produced oxide layer on the surface of the alloy is more protected. Additionally, they reveal that the values of R_b are higher than R_p at the same annealing temperatures (Table 5), suggesting that the barrier layer has a high resistance to transporting both the charge and the species across it. Because there are slightly more processes of corrosion, R_p and R_b values are lower at annealing temperatures (1000 °C) than they are at 600 and 800 °C. When the annealing temperature is raised (between 600 and 800 °C), the CPE_p and CPE_b drop, suggesting that the two oxide films thickness has risen. At the same temperatures, the CPE_p is higher than the CPE_b, proving that the barrier oxide layer is in charge of the resistance to corrosion. The CPE_p and CPE_b values at annealing temperatures of 1000 °C are higher than they are between 600 and 800 °C, showing that the two oxide layers thickness is reduced. This outcome indicates that the two oxide layers thickness decreases at higher annealing temperatures as a result of their dissolution [42].

3.4.3 Corrosion Resistance Resulted from OCP

Figure 7 depicts the OCP of the $T_{70}Z_{20}N_{7.5}T_{2.5}$ alloy without and with annealing at various temperatures in a RS as a function of time. Generally, annealed samples at 600 and 800 °C possess a higher positive potential in comparison with those that are unannealed or annealed at 1000 °C. For the unannealed sample, shortly after the potential decreases, the OCP rapidly rises to a more positive potential, indicating that it may re-passivate rapidly. A steady-state value of -0.31 V was eventually reached. And for those annealed at 800 °C, the OCP increases in the positive trend, reaching a maximum steady-state value at – 0.03 V, a very long and stable passive region. During the immersion of the annealed samples at 600 and 1000 °C, the potential initially changed in a negative direction. The local breakdown of the passive film, which in turn resulted from the initial the initial dissolving of the native passivation layer on the titanium alloy surface, was most likely what caused this change in the negative trend. The curves finally attain a stable state after a certain amount of time. This might be as a result of the development of a new passivation coat in RS, which slowed down the rate of OCP change. The potential was stabilized when the passivation layer dissolved and produced a prorated balance [43]. At varying annealing temperatures, the $T_{70}Z_{20}N_{7.5}T_{2.5}$

Table 5 Fitting parameters of EIS obtained for the $T_{70}Z_{20}N_{7.5}T_{2.5}$ alloy annealed at different temperatures in a RS

Temperature °C	R_s (Ω cm^2)	R_b (kΩ cm^2)	CPE_b (F cm^2 $H_Z{}^{1-n1}$)	n $_1$	R_p (Ω cm^2)	CPE_p (F cm^2 $H_Z{}^{1-n2}$)	n $_2$
Unannealed	44.56	31.59×10^3	45.60×10^{-6}	0.842	45.79	147.2×10^{-6}	0.895
600	24.93	64.05×10^3	34.20×10^{-6}	0.803	51.98	88.18×10^{-6}	0.872
800	18.55	112.3×10^3	28.69×10^{-6}	0.821	68.56	60.45×10^{-6}	0.852
1000	33.54	9.78×10^3	134.17×10^{-6}	0.758	14.24	277.35×10^{-6}	0.741

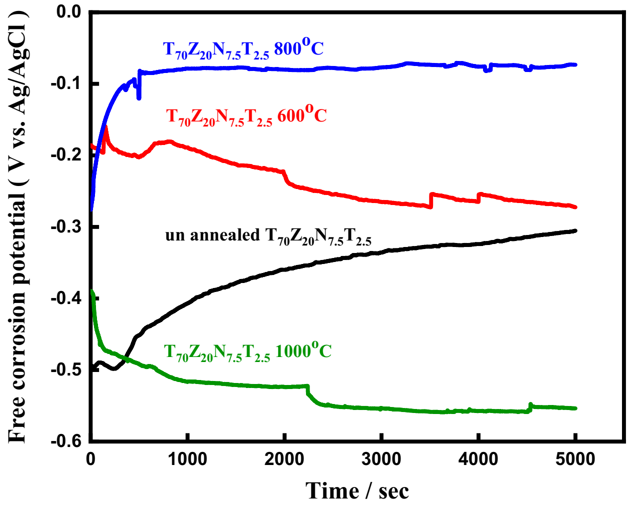

Fig. 7 Open-circuit potential behavior as a function of time for $T_{70}Z_{20}N_{7.5}T_{2.5}$ samples without and with annealing at different temperatures

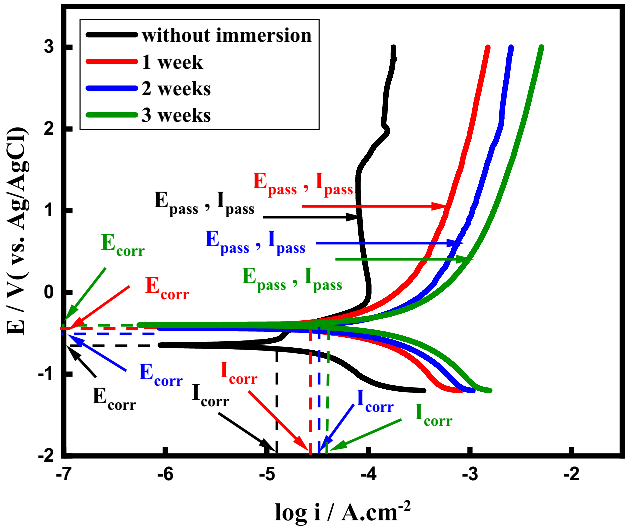

Fig. 8 Potentiodynamic polarization curves of $T_{70}Z_{20}N_{7.5}T_{2.5}$ alloy in a RS at various immersion times with a scan rate of 5 mVs^{-1} at 37 °C

alloy has a varied final steady-state potential. Figure 7 shows that the OCP of the $T_{70}Z_{20}N_{7.5}T_{2.5}$ alloy ranges from − 0.03 to − 0.55 V after being annealed at various temperatures. In spite of the fact that the trends of change of OCP for sample $T_{70}Z_{20}N_{7.5}T_{2.5}$ annealed at various temperatures were comparable, they varied in the time required to attain steady state. Additionally, the alloy that was annealed at 800 °C exhibited the highest potential, attaining − 0.03 V. The potential value of the sample annealed at 600 °C was lower, at − 0.27 V, while the sample annealed at 1000 °C had the lowest potential, at approximately − 0.55 V. These data demonstrate that the sample $T_{70}Z_{20}N_{7.5}T_{2.5}$ annealed at 800 °C had the greatest resistance to corrosion when compared to the samples annealed at 600 °C and unannealed, and when it was annealed at 1000 °C the resistance to corrosion was the worst. Therefore, it is recommended to anneal the $T_{70}Z_{20}N_{7.5}T_{2.5}$ alloy at 800 °C to improve its corrosion resistance.

3.5 Impact of Immersion Time

3.5.1 Corrosion Resistance Resulted from PPCs

Figure 8 illustrates the PPCs of the $T_{70}Z_{20}N_{7.5}T_{2.5}$ alloy in a RS without and with various immersion times, at 37 °C with a 5-mVs^{-1} scan rate. As the immersion time increases from one week to three weeks, the dissolution of the passive film generated on the surface of the alloy becomes easier. Without immersion, the polarization curves behave in an active–passive manner and are moved toward a less noble potential, which indicates a reduction in the resistance to corrosion of the $T_{70}Z_{20}N_{7.5}T_{2.5}$ sample. The active–passive transition behavior may be seen in the polarization curves of the $T_{70}Z_{20}N_{7.5}T_{2.5}$ alloy at various immersion times. The current density rises quickly when the potential rises. This is probably attributed to the destruction of the native passive layer of the $T_{70}Z_{20}N_{7.5}T_{2.5}$ alloy, which led to the active dissolution behavior of the alloy. When the potential was greater than 0.20 V, the current density rose and entered the stable passive area. This may be the result of the surface producing a new passive film to protect the alloy. The current density has reached a stable state, when the balance between the production and degradation of the passive layer has been achieved [44]. The polarization curves with immersion are moved toward nobler potentials comparable to the polarization curves without immersion. This might be explained by the rapid cathodic reaction. (The right branch of the polarization curve). Using the following parameters, the corrosion behavior was estimated: I_{corr}, $E_{corr,}$ I_{pass}, and CR (Table 6). It could be deduced that the resistance to corrosion of the alloy is greater without immersion than it is with immersion because the values of I_{corr}, I_{pass}, and CR are lower without immersion than they are with immersion. The sample at one

Table 6 Electrochemical parameters obtained for a $T_{70}Z_{20}N_{7.5}T_{2.5}$ alloy in a RS with various immersion times at 37 °C

Immersion time Week	I_{Corr} A cm^{-2}	-E_{Corr} V	I_{pass} mA cm^{-2}	Corr Rate mpy
Without immersion	1.18×10^{-5}	0.558	0.114	6.10
One week	2.47×10^{-5}	0.416	0.336	12.18
Two weeks	2.82×10^{-5}	0.435	0.594	14.65
Three weeks	3.31×10^{-5}	0.400	0.886	17.15

week of immersion time exhibits an I_{corr} value (3.76×10^{-5} A cm^{-2}) lower than the values of the other two samples (4.70×10^{-5} and $5.80\times10^{-5}Acm^{-2}$, respectively) and, as a result, this sample is therefore more resistant to corrosion than the other two samples. The lower I_{pass} implies that a stable passive film is formed. At the one week of immersion, the sample exhibit the lowest I_{pass} value, indicating the formation of a highly stable passive film. The CR value of the sample at three weeks of immersion is higher than that of the two other samples (at one and two weeks of immersion times), which indicates that this sample has the lowest corrosion resistance and displays that the CR enhances with longer immersion times.

3.5.2 Corrosion Resistance Resulted from EIS

Figures 9a and b report the EIS examinations of the $T_{70}Z_{20}N_{7.5}T_{2.5}$ alloy, without and with various immersion times in a RS at 37 °C. According to Nyquist plots (Fig. 9a), the capacitive semicircle value is higher without immersion than it is with immersion and the semicircle values get smaller with an increase in the immersion time. These outcomes show that the $T_{70}Z_{20}N_{7.5}T_{2.5}$ sample's resistance to corrosion reduces as the time of immersion increases and is higher without immersion than with immersion. Bode plots (Fig. 9b) show that without immersion, the Z_{mod} value (28.18 kΩ cm^2) and phase angle (− 67.88°) are greater than when immersed. This suggests that the passive oxide coating is more protective without immersion than it is with immersion. As the immersion time increased, the Z_{mod} values fell from 14.45 to 0.776 kΩ cm^2. In addition, phase angles fall from − 68.59° to − 50.96°. These outcomes show that the oxide layer on the $T_{70}Z_{20}N_{7.5}T_{2.5}$ alloy dissolves rapidly as immersion time in a RS is increased. In the examination of the EIS acquired at the OCP, it was observed that the entire data collection for the sample could be successfully fitted with the equivalent circuit shown in Fig. 3 after evaluating a variety of various electrical circuit models. A two-layer model of the surface coating is used to support this. Table 7 contains the parameters (Rs, Rp, CPEp, Rb, and CPEb) of the suggested equivalent circuit obtained for $T_{70}Z_{20}N_{7.5}T_{2.5}$ alloy without and with various immersion times in a RS. The results show that R_p and R_b decrease as immersion time in RS increases, indicating that the developed oxide coating on $T_{70}Z_{20}N_{7.5}T_{2.5}$ becomes less resistant as immersion time in RS increases. However, R_b is significantly larger than R_p. This suggests that the protection is supplied by the inner layer and is comparable with what Assis et al. reported for

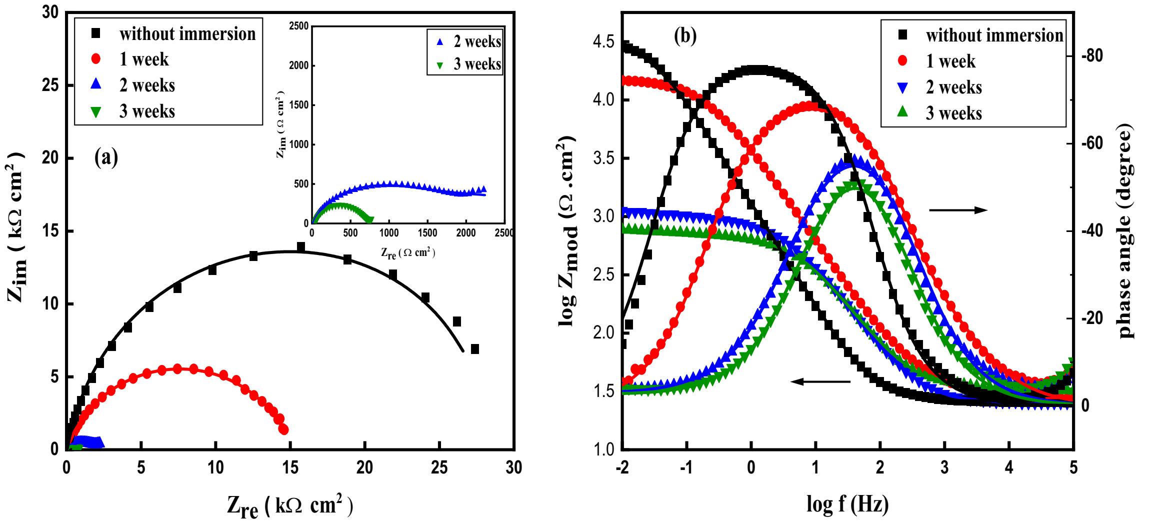

Fig. 9 Nyquist diagrams (**a**) and Bode plots (b) of $T_{70}Z_{20}N_{7.5}T_{2.5}$ alloy at open-circuit potential in a RS at various immersion times at 37 °C

Table 7 Fitting parameters of EIS obtained for a $T_{70}Z_{20}N_{7.5}T_{2.5}$ alloy in RS with various immersion times at 37 ºC

Immersion time/Week	R_s (Ω cm^2)	R_b (Ω cm^2)	CPE_b (F cm^2 H_Z^{1-n1})	n_1	R_p (kΩ cm^2)	CPE_p (F cm^2 H_Z^{1-n2})	n_2
Without immersion	44.56	31.59×10^3	45.60×10^{-6}	0.842	45.79	147.2×10^{-6}	0.895
1 week	26.00	14.86×10^3	49.33×10^{-6}	0.791	16.95	167.9×10^{-6}	0.846
2 weeks	17.34	2.409×10^3	59.23×10^{-6}	0.798	2.656	198.2×10^{-6}	0.782
3 weeks	14.79	1.140×10^3	83.02×10^{-6}	0.810	1.453	204.3×10^{-6}	0.756

Ti alloys [45]. The CPE_p and CPE_b enhance with longer times of immersion, showing that the thickness of two oxide coatings has reduced as a result of their dissolution at high immersion times. CPE_p is greater than CPE_b, indicating that the inner oxide coating is in charge of resistance to corrosion.

3.5.3 Corrosion Resistance Resulted from OCP

Figure 10 shows the variations in the free corrosion potential of the $T_{70}Z_{20}N_{7.5}T_{2.5}$ alloy in a RS at various immersion times. The behavior of the potential time is completely changed with immersion. For the studied alloy, the OCP changed dramatically from − 0.49 V at the beginning to − 0.34 V at the end of the measurement. As the immersion time is increased from one week to three weeks, it is possible that the dissolution of the passive layer becomes easier. The steady-state potential is achieved in a short time after immersion in RS, in comparison with those without immersion time. In all the samples within the first several minutes of immersion, the potential was initially slightly negative. The local passive layer on the $T_{70}Z_{20}N_{7.5}T_{2.5}$ alloy surface was dissolved at the initial step, which led to this shift in the negative trend. Eventually, after a certain amount of time, the curves reach a steady state. This might be attributed to the production of a new passive coating, slowing the rate at which the OCP changes. The potential becomes stable when the passivation coating disintegration rate and production are relatively balanced [43].

At various immersion times, the final steady-state potential of the $T_{70}Z_{20}N_{7.5}T_{2.5}$ alloy varies. Additionally, the alloy that had been submerged for one week had the highest potential, measuring about − 0.35 V. The alloy immersed for two weeks had a lower potential, measuring about − 0.38. The alloy immersed for three weeks had the least potential, measuring about − 0.42 V. These data reveal that the $T_{70}Z_{20}N_{7.5}T_{2.5}$ alloy immersed for one week has greater resistance two corrosions compared to the alloys immersed for two and three weeks, suggesting that the $T_{70}Z_{20}N_{7.5}T_{2.5}$ alloy corrosion resistance increases as the immersion time decreases.

3.6 Microstructural Properties

An XRD structural investigation was carried out to understand the composition of phases and the microstructure of the $T_{70}Z_{20}N_{7.5}T_{2.5}$ sample. In Fig. 11, the X-ray diffractograms for $T_{70}Z_{20}N_{7.5}T_{2.5}$ samples without and with annealing at various temperatures are displayed. The relationship between the diffraction angle (2θ) and the relative intensity (counts per second) is graphed. The peaks of the unannealed $T_{70}Z_{20}N_{7.5}T_{2.5}$ alloy are indexed to the (100), (002), (101), (102), (110), and (103) planes at 2θ values of 34.1, 37.6, 38.7, 50.0, 61.6, and 68.6°, respectively. These peaks correspond to those of the hexagonal α-Ti. The two peaks that appeared at $2\theta = 37.6$ and 68.6° are due to the (110) and (211) levels of the β-Ti phase, respectively [46]. The results also found that the (101) plane was the most common crystallographic orientation for the hexagonal Ti phase. Using Scherrer formula (2) [47] and the (101) peak, the grain size of α phase was calculated to be 5.35 nm. Other TiZrNbTa alloys showed comparable results [48].

$$D = \frac{0.9\lambda}{\beta \cos\theta}, \tag{2}$$

where D is the grain size, λ is the wavelength of the diffraction X-ray, β is the full-width at half-maximum of the diffraction peak, and θ is the angle of diffraction. There were

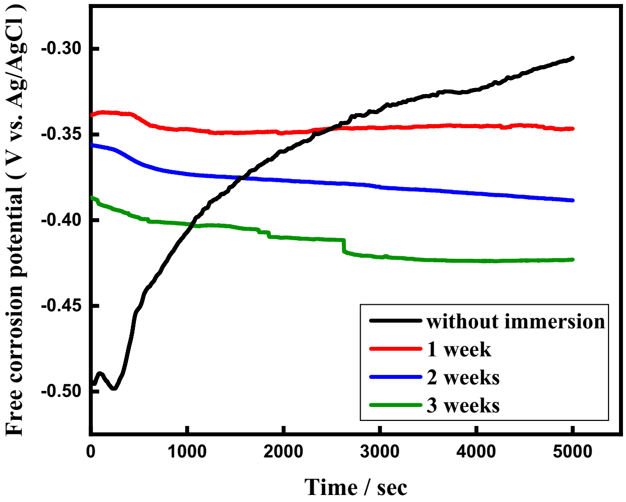

Fig. 10 Variation of $T_{70}Z_{20}N_{7.5}T_{2.5}$ alloy open-circuit potential in a RS at various immersion times at 37 °C

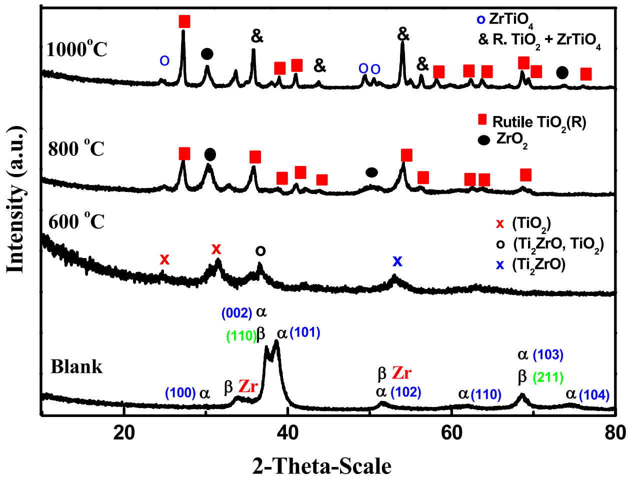

Fig. 11 The X-ray diffraction analysis obtained for the $T_{70}Z_{20}N_{7.5}T_{2.5}$ alloy without and with annealing at different temperatures

no oxide peaks found in the unannealed sample, and all of the diffraction peaks were connected to body-centered Ti and hexagonal close-packed Ti, indicating that the naturally produced Titania films were amorphous, despite the tendency of titanium alloys to generate TiO_2 films at ambient temperature [49].

When the alloy samples were compared after being annealed at 600, 800, and 1000 °C, it was revealed that annealing at 600 °C resulted in the appearance of new peaks at 2θ values of 25.4, 31.5, 36.2, 53.71, and 63.7° (JCPDS No. 00-027-0911), which are consistent with those of the orthorhombic TiO_2 (JCPDS No. 01-084-1750), as well as two peaks of orthorhombic Ti_2ZrO at 36.2 and 63.7° (JCPDS No. 00-027-0911). However, when annealing at 800 °C, additional peaks that are compatible with those of rutile, syn tetragonal TiO_2, and cubic ZrO_2 are formed (JCPDS No. 01-076-0320 and 00-027-0997, respectively). However, annealing at 1000 °C, the same peaks that are comparable with those of rutile, syn tetragonal TiO_2, and cubic ZrO_2 appeared, as well as new peaks which are comparable with those of $ZrTiO_4$ (JCPDS No. 00-034-0415). Figure 11 shows that the annealing altered the crystallization of the oxide, i.e., the amorphous oxide turns into the crystalline rutile TiO_2. Better corrosion resistance and biocompatibility would be provided by implants with a crystalline rutile layer rather than an amorphous TiO_2 layer [50].

3.7 Surface Morphology

The surface morphology of the polished (Fig. 12a) as well as the alloy samples at different immersion times and at different annealing temperatures is shown in Fig. 12. Increasing the immersion times (Fig. 12b, c, d) leads to surface defects as a result of possible dissolution of the passive layer, especially after three weeks in comparison with the unimmersed sample. Increasing the annealing temperatures from 600 to 800 °C, on the other hand, changed the morphology from amorphous to crystalline, as confirmed by the XRD patterns (Fig. 10). Annealing at 1000 °C causes microcracks to form, resulting in a less proactive (i.e., less corrosion resistant) surface. The presence of some small pits on the surface does not represent a big problem since there is less tendency for the alloy to pit, as shown from the polarization curves studied in Figs. 5 and 8, which do not refer to pitting in the potential range studied.

4 Conclusion

In this study, the in vitro corrosion resistance of the $T_{70}Z_{20}N_{7.5}T_{2.5}$ alloy has been evaluated and contrasted with that of T_6A_4V and Ti in RS. Electrochemical studies were used to examine the corrosion behavior of the $T_{70}Z_{20}N_{7.5}T_{2.5}$ alloy when it was annealed at 600, 800, and 1000 °C and immersed for various immersion times. The data in this work led to the following conclusions:

1) The Z_{mod} and R_b values of $T_{70}Z_{20}N_{7.5}T_{2.5}$ alloy (28.18 kΩ cm^2 and 31.59×10^3 kΩ cm^2, respectively) is greater than those of T_6A_4V alloy (16.60 kΩ cm^2 and 28.46×10^3 kΩ cm^2, respectively) and Ti (6.92 kΩ cm^2 and 17.14×10^3 kΩ cm^2, respectively), indicating that the spontaneous oxide coating for $T_{70}Z_{20}N_{7.5}T_{2.5}$ alloy has improved in its ability to resist corrosion. According to PPC's results, the I_{corr} value of the $T_{70}Z_{20}N_{7.5}T_{2.5}$ alloy ($I_{corr} = 11.8$ μA cm^{-2}) is also smaller compared to T_6A_4V ($I_{corr} = 13.7$ μA cm^{-2}) and Ti ($I_{corr} = 29.5$ μA cm^{-2}). Both EIS and PPCs data show that $T_{70}Z_{20}N_{7.5}T_{2.5}$ has the highest level of corrosion resistance comparable to those of the T_6A_4V alloy and Ti.
2) In contrast to the T_6A_4V (OCP = − 0.35 V) and Ti (OCP = − 0.48 V) samples, the values of OCP for the $T_{70}Z_{20}N_{7.5}T_{2.5}$ sample became more positive with time (− 0.30 V) indicating that the $T_{70}Z_{20}N_{7.5}T_{2.5}$ is in a state of greatly stable passivation and is highly resistant to corrosion.
3) In comparison to the other samples, including annealed and unannealed ones, the $T_{70}Z_{20}N_{7.5}T_{2.5}$ alloy showed the best corrosion resistance when it was annealed at a temperature of 800 °C. The $T_{70}Z_{20}N_{7.5}T_{2.5}$ alloy annealed at 1000 °C had the greatest I_{pass}, (0.611 mA cm^{-2}), whereas the alloy annealed at 800 °C had the lowest I_{pass} (0.009 mA cm^{-2}).
4) The EIS results display that the passive film is composed of a dual-outer and inner oxide layer and that at a critical high temperature (up to 800 °C) the resistance of corrosion of the $T_{70}Z_{20}N_{7.5}T_{2.5}$ sample increases, but above this critical temperature (at 1000 °C) and without annealing, the resistance of corrosion decreases due to the dissolution process of the passive film on the $T_{70}Z_{20}N_{7.5}T_{2.5}$ sample surface.
5) The OCP data show that the resistance to corrosion of the $T_{70}Z_{20}N_{7.5}T_{2.5}$ sample treated at 800 °C (-0.03 V) was the best in comparison to the untreated and annealed samples at 600 °C (-0.31, -0.27 V, respectively) and the resistance to corrosion was the least when the alloy was treated at 1000 °C (-0.55 V).
6) The PPCs data show that without immersion, the alloy corrosion resistance is higher than its value both with immersion and with decreasing the immersion time. These results agree with the EIS and OCP data of the alloy at the same immersion times.
7) The $T_{70}Z_{20}N_{7.5}T_{2.5}$ system was discovered to have a structure made up of alpha- and beta-phases. An examination of the X-ray structure found a combination of hexagonal close-packed α-Ti (main phase, with 5.35-nm

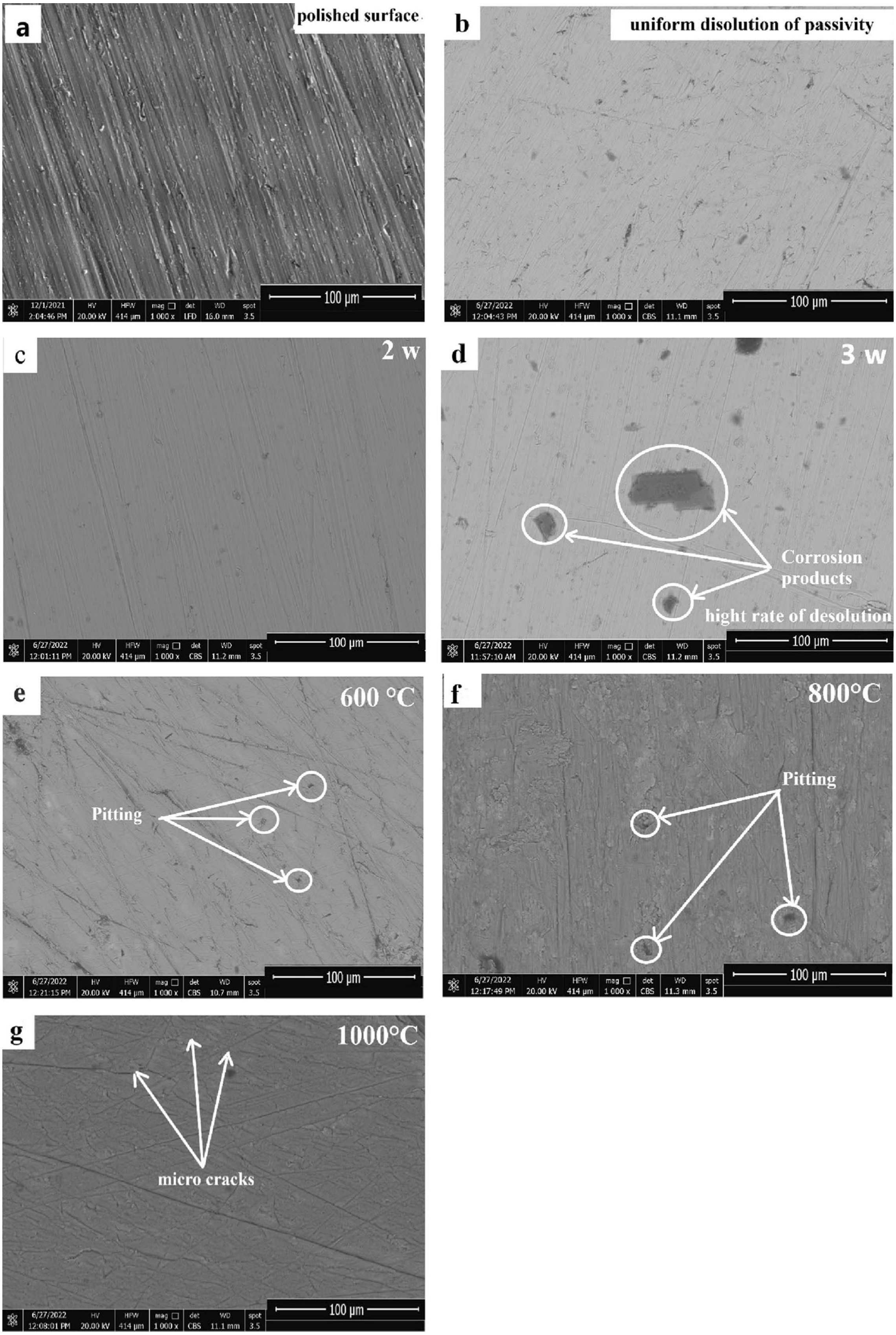

Fig. 12 SEM images of the $T_{70}Z_{20}N_{7.5}T_{2.5}$ sample surface at different immersion times in RS at 37 °C **a** blank, **b** one week, **c** two weeks, **d** three weeks, and samples annealed at different temperatures **e** 600, **f** 800 °C, and **g** 1000 °C

grain size) and body-centered Ti. Of all the materials investigated in this work, the alloy $T_{70}Z_{20}N_{7.5}T_{2.5}$ can be regarded as a promising material appropriate for use as a biomaterial.

Author Contributions All authors contributed to the study conception and design. Material preparation, data collection, and analysis were performed by IHE, MAMI, and NFEB. The first draft of the manuscript was written by all authors commented on previous versions of the manuscript. All authors read and approved the final manuscript.

Funding The authors declare that no funds, grants, or other support were received during the preparation of this manuscript.

Data Availability All data generated or analyzed during this study are included in this published article.

Declarations

Conflict of interest The authors declare that they have no conflicts of interest.

Ethics Approval Not Applicable.

Consent to Participate Not Applicable.

Consent for Publication Not Applicable.

References

1. Pricopi MM, Chelariu RO, Apostolescu NI, Gordin DM, Sutiman DA, Mareci DA (2020) Corrosion behavior of some timonb alloys in ringer solution. Revista de Chimie-Bucharest-Original Ed 71(7):187–96. https://doi.org/10.37358/RC.20.7.8236
2. Radovanović MB, Tasić ZZ, Simonović AT, Petrović Mihajlović MB, Antonijević MM, (2020) Corrosion behavior of titanium in simulated body solutions with the addition of biomolecules. ACS Omega 5(22):12768–12776. https://doi.org/10.1021/acsomega.0c00390
3. Xue C, Zhang P, Wei D, Hu H, Li F, Yang K (2020) Corrosion and Tribocorrosion behaviors for TA3 in Ringer's Solution after Implantation of Nb Ions. Appl Sci 10(23):8329. https://doi.org/10.3390/app10238329
4. Lira Martinez MA, Almeraya F, Jaquez J, Gaona Tiburcio C, Estupiñan F, Cabral J, Zambrano P (2022) Corrosion behavior of titanium and titanium alloys in Ringer´s Solution. Int J Electrochem Sci 17:55. https://doi.org/10.20964/2022.07.55
5. Li Z, Lai W, Wang B, Tong X, You D, Li W, Wang X (2022) A novel Ti42. 5Zr42. 5Nb5Ta10 multi-principal element alloy with excellent properties for biomedical applications. Intermetallics. 151:107731. https://doi.org/10.3390/ma15113938
6. Yang HL, Juaim AN, Zou L, Zhu MZ, Chen XN, Ma CX, Zhou XW (2022) Antibacterial activity and mechanism of newly developed Zr-30Ta and Zr-25Ta-5Ti alloys against implant-associated infection. Rare Met 41(12):4176–4187. https://doi.org/10.1007/s12598-022-02144-5
7. Jawed SF, Rabadia CD, Khan MA, Khan SJ (2022) Effect of alloying elements on the compressive mechanical properties of biomedical titanium alloys: a systematic review. ACS Omega 7(34):29526–42. https://doi.org/10.1021/2Facsomega.2c02096
8. Zhao K, Wu H, Xiao C, Dong J, Ren J, Peng Z (2022) Study on corrosion resistance and biological properties of the double glow plasma Nb-Zr biological implantation alloying layers. Coatings 12(7):942. https://doi.org/10.3390/coatings12070942
9. Wang YB, Zheng YF (2009) Corrosion behaviour and biocompatibility evaluation of low modulus Ti–16Nb shape memory alloy as potential biomaterial. Mater Lett 63(15):1293–1295. https://doi.org/10.1016/j.matlet.2009.02.062
10. Trillo EA, Ortiz C, Dickerson P, Villa R, Stafford SW, Murr LE (2001) Evaluation of mechanical and corrosion biocompatibility of TiTa alloys. J Mater Sci - Mater Med 12(4):283–292. https://doi.org/10.1023/A:1011210101895
11. Wen CE, Yamada Y, Hodgson PD (2006) Fabrication of novel TiZr alloy foams for biomedical applications. Mater Sci Eng, C 26(8):1439–1444. https://doi.org/10.1016/j.msec.2005.08.006
12. Geetha M, Singh AK, Asokamani R, Gogia AK (2009) Ti based biomaterials, the ultimate choice for orthopaedic implants–a review. Prog Mater Sci 54(3):39. https://doi.org/10.1016/j.pmatsci.2008.06.004
13. Assis SL, Wolynec S, Costa I (2008) The electrochemical behaviour of Ti-13Nb-13Zr alloy in various solutions. Mater Corros 59(9):739–743. https://doi.org/10.1002/maco.200804148
14. Bottino MC, Coelho PG, Henriques VA, Higa OZ, Bressiani AH, Bressiani JC (2009) Processing, characterization, and in vitro/in vivo evaluations of powder metallurgy processed Ti-13Nb-13Zr alloys. J Biomed Mater Res 88(3):689–696. https://doi.org/10.1002/jbm.a.31912
15. Ruan JM, Grant MH (2001) Biocompatibility evaluation in vitro. Part III: cytotoxicity expression of human and animal osteoblasts on the biomaterials. J Cent South Univ Technol 8(3):147–55. https://doi.org/10.1007/s11771-001-0044-1
16. Hamdy AS, El-Shenawy E, El-Bitar T (2006) Electrochemical impedance spectroscopy study of the corrosion behavior of some niobium bearing stainless steels in 3.5% NaCl. Intern J Electrochem Sci 1(4):171–80
17. Sherepo KM, Red'ko IA (2004) The use of zirconium for implants in traumatology and orthopedics. Med Tekh 2:22–24
18. Cabrini RL, Guglielmotti MB, Almagro JC (1993) Histomorphometry of initial bone healing around zirconium implants in rats. Implant Dent 2(4):264–7. https://doi.org/10.1097/00008505-199312000-00008
19. Kulakov OB, Doktorov AA, D'iakova SV, Grötz KA (2005) Experimental study of osseointegration of zirconium and titanium dental implants. Morfologiia 127(1):52–5
20. Robin A, Rosa JL (2000) Corrosion behavior of niobium, tantalum and their alloys in hot hydrochloric and phosphoric acid solutions. Intern J Refrac Metals Hard Mater 18(1):13–21. https://doi.org/10.1016/S0263-4368(99)00034-7
21. Yang HP, Yang SH, Cai YN, Hou GF, Xia JY, Tang MT (2011) Electrochemical behaviors of tantalum in anhydrous ethanol containing hydrogen sulfate ions. Trans Nonferrous Metals Soc China 21(1):179–184. https://doi.org/10.1016/S1003-6326(11)60696-1
22. Matsuno H, Yokoyama A, Watari F, Uo M, Kawasaki T (2001) Biocompatibility and osteogenesis of refractory metal implants, titanium, hafnium, niobium, tantalum and rhenium. Biomaterials 22(11):1253–1262. https://doi.org/10.1016/S0142-9612(00)00275-1
23. Li J, Zhou L, Li Z (2010) Corrosion behaviors of a new titanium alloy TZNT for surgical implant application in Ringer's solution. Rare Met 29(1):37–44. https://doi.org/10.1007/s12598-010-0007-5
24. Gurappa I (2002) Characterization of different materials for corrosion resistance under simulated body fluid conditions. Mater Charact 49(1):73–79. https://doi.org/10.1016/S1044-5803(02)00320-0

25. Mashtalyar DV, Nadaraia KV, Imshinetskiy IM BEA, Sinebrukhov SL, Gnedenkov SV (2022) Features of composite layers created using an aqueous suspension of a fluoropolymer. Polymers 14:4667. https://doi.org/10.3390/polym14214667
26. Egorkin VS, Mashtalyar DV, Gnedenkov AS, Filonina VS, Vyaliy IE, Nadaraia KV, Imshinetskiy IM, Belov EA, Izotov NV, Sinebryukhov SL et al (2021) Icephobic performance of combined fluorine-containing composite layers on Al-Mg-Mn–Si alloy surface. Polymers 13:3827. https://doi.org/10.3390/polym13213827
27. Mosab K, Tehseen Z, Burak D, Ali D, Arash FA (2022) A novel dual-functional layer exhibiting exceptional protection and photocatalytic activity by organic functionalization of plasma electrolyzed layer. J Magnes Alloys. https://doi.org/10.1016/j.jma.2022.10.004
28. Mansfeld F (2007) The interaction of bacteria and metal surfaces. Electrochim Acta 52(27):7670–7680. https://doi.org/10.1016/j.electacta.2007.05.006
29. Elshamy IH, Ibrahim MA, Abdel Rehim SS, El Boraei NF (2023) Electrochemical characteristics of a biomedical Ti70Zr20Nb7.5Ta2. 5 refractory high entropy alloy in an artificial saliva solution. J Bio- Tribo-Corros 9(1):1–7. https://doi.org/10.1007/s40735-022-00726-5
30. Wang BL, Zheng YF, Zhao LC (2009) Electrochemical corrosion behavior of biomedical Ti–22Nb and Ti–22Nb–6Zr alloys in saline medium. Mater Corros 60(10):788–794. https://doi.org/10.1002/maco.200805173
31. Assis SL, Costa IS (2007) Electrochemical evaluation of Ti-13Nb-13Zr, Ti-6Al-4V and Ti-6Al-7Nb alloys for biomedical application by long-term immersion tests. Mater Corros 58(5):329–333. https://doi.org/10.1002/maco.200604027
32. Tamilselvi S, Raman V, Rajendran N (2006) Corrosion behaviour of Ti–6Al–7Nb and Ti–6Al–4V ELI alloys in the simulated body fluid solution by electrochemical impedance spectroscopy. Electrochim Acta 52(3):839–846. https://doi.org/10.1016/j.electacta.2006.06.018
33. Alves VA, Reis RQ, Santos IC, Souza DG, Gonçalves TD, Pereira-da-Silva MA, Rossi A, Da Silva LA (2009) In situ impedance spectroscopy study of the electrochemical corrosion of Ti and Ti–6Al–4V in simulated body fluid at 25 $^{\circ}$C and 37 $^{\circ}$C. Corros Sci 51(10):2473–2482. https://doi.org/10.1016/2Fj.corsci.2009.06.035
34. Karthega M, Raman V, Rajendran N (2007) Influence of potential on the electrochemical behaviour of β titanium alloys in Hank's solution. Acta Biomater 3(6):1019–1023. https://doi.org/10.1016/j.actbio.2007.02.009
35. Rosalbino F, Maccio D, Scavino G, Saccone A (2012) In vitro corrosion behaviour of Ti–Nb–Sn shape memory alloys in Ringer's physiological solution. J Mater Sci - Mater Med 23(4):865–871. https://doi.org/10.1007/s10856-012-4560-3
36. Mareci D, Ungureanu G, Aelenei DM, Rosca JM (2007) Electrochemical characteristics of titanium based biomaterials in artificial saliva. Mater Corros 58(11):848–856. https://doi.org/10.1002/maco.200704065
37. Qu Q, Wang L, Chen Y, Li L, He Y, Ding Z (2014) Corrosion behavior of titanium in artificial saliva by lactic acid. Materials 7(8):5528–5542. https://doi.org/10.3390/ma7085528
38. Ibrahim MA, Korablov SF, Yoshimura M (2002) Corrosion of stainless steel coated with TiN,(TiAl) N and CrN in aqueous environments. Corros Sci 44(4):815–828. https://doi.org/10.1016/S0010-938X(01)00102-0
39. El Boraei NF, Ibrahim MA (2020) Comparative study on the corrosion behaviour of lord razor blade steel (LRBS) in aqueous environments. J Taibah Univ Sci 14(1):423–436. https://doi.org/10.1080/16583655.1742473
40. Elshamy IH, Abd El Rehim SS, Ibrahim MAM, El Boraei NF (2022) The bifunctional role played by thiocyanate anions on the active dissolution and the passive film of titanium in hydrochloric acid. Corros Eng Sci Technol 57(6):542–552. https://doi.org/10.1080/1478422X.2022.2099334
41. Ibrahim MA, Pongkao D, Yoshimura M (2002) The electrochemical behavior and characterization of the anodic oxide film formed on titanium in NaOH solutions. J Solid State Electrochem 6(5):341–350. https://doi.org/10.1007/s100080100229
42. Robin A, Meirelis JP (2009) EIS study of Ti–23Ta alloy in artificial saliva. Corros Eng, Sci Technol 44(5):352–357. https://doi.org/10.1179/147842208X338992
43. Yu SY, Scully JR (1997) Corrosion and passivity of Ti-13% Nb-13% Zr in comparison to other biomedical implant alloys. Corrosion 53(12):965–976. https://doi.org/10.5006/1.3290281
44. Wang ZB, Hu HX, Zheng YG, Ke W, Qiao YX (2016) Comparison of the corrosion behavior of pure titanium and its alloys in fluoride-containing sulfuric acid. Corros Sci 103:50–65. https://doi.org/10.1016/2Fj.corsci.2015.11.003
45. Assis SL, Wolynec S, Costa I (2006) Corrosion characterization of titanium alloys by electrochemical techniques. Electrochim Acta 51(8–9):1815–1819. https://doi.org/10.1016/j.electacta.2005.02.121
46. Vladescu A, Braic V, Balaceanu M, Braic M, Parau AC, Ivanescu S, Fanara C (2013) Characterization of the Ti-10Nb-10Zr-5Ta alloy for biomedical applications. Part 1: microstructure, mechanical properties, and corrosion resistance. J Mater Engi Performance 22(8):2389–2397. https://doi.org/10.1007/s11665-013-0517-z
47. Klug HP, Alexander LE (1974) Procedures XR. John Wiley, New York, pp 687–703
48. Raducanu D, Vasilescu E, Cojocaru VD, Cinca I, Drob P, Vasilescu C, Drob SI (2011) Mechanical and corrosion resistance of a new nanostructured Ti–Zr–Ta–Nb alloy. J Mech Behav Biomed Mater 4(7):1421–1430. https://doi.org/10.1016/j.jmbbm.2011.05.012
49. Hynowska A, Pellicer E, Fornell J, Gonza'lez S, van Steenberge N, Surin˜ach S, Gebert A, Calin M, Eckert J, Dolors Baro M, Sort J (2012) Nanostructured b-phase Ti-31.0Fe-9.0Sn and Sub-lm structured Ti-39.3Nb-13.3Zr-10.7Ta alloys for biomedical applications, microstructure benefits on the mechanical and corrosion performances. Mater Sci Eng C 32:2418–2425. https://doi.org/10.1016/j.msec.2012.07.016
50. Forsgren J, Svahn F, Jarmar T, Engqvist H (2007) Formation and adhesion of biomimetic hydroxyapatite deposited on titanium substrates. Acta Biomater 3(6):980–984. https://doi.org/10.1016/j.actbio.2007.03.006